

## Development of an outdoor MRI system for measuring flow in a living tree



Akiyoshi Nagata, Katsumi Kose, Yasuhiko Terada\*

Institute of Applied Physics, University of Tsukuba, Tsukuba, Ibaraki, Japan

### ARTICLE INFO

#### Article history:

Received 13 October 2015

Revised 4 February 2016

Available online 11 February 2016

#### Keywords:

Outdoor MRI system

Living tree

Flow

q-space imaging

### ABSTRACT

An outdoor MRI system for noninvasive, long-term measurements of sap flow in a living tree in its natural environment has been developed. An open-access, 0.2 T permanent magnet with a 160 mm gap was combined with a radiofrequency probe, planar gradient coils, electromagnetic shielding, several electrical units, and a waterproofing box. Two-dimensional cross-sectional images were acquired for a ring-porous tree, and the anatomical structures, including xylem and phloem, were identified. The MRI flow measurements demonstrated the diurnal changes in flow velocity in the stem on a per-pixel basis. These results demonstrate that our outdoor MRI system is a powerful tool for studies of water transport in outdoor trees.

© 2016 Elsevier Inc. All rights reserved.

### 1. Introduction

A major advantage of magnetic resonance imaging (MRI) is its capability of acquiring data from the interior of a living sample in a nondestructive manner. This advantage has opened up a wide variety of applications in plant sciences. Technological developments in plant MRI have now enabled the investigation of root and stem anatomy, and of water content and transport in roots, stems, and leaves (see, e.g., Refs. [1,2] and references therein).

Until now, most MRI studies on intact plants have been performed in laboratories or greenhouses using plants that were in pots or vessels. These indoor measurements have been performed in a physiologically controlled environment and have provided valuable information on plant physiology and development in relation to the controlled environment. In contrast, outdoor MRI measurements are superior to indoor ones in some respects. Importantly, outdoor MRI allows the monitoring of physiological processes of plants growing in their natural environment, which is very difficult to achieve in laboratories or greenhouses. Moreover, the size of the plants to be measured is not limited by the size of the laboratory or greenhouse, and larger trees can be investigated.

However, there are numerous difficulties in the use of MRI systems outdoors. For example, the MRI system should be robust enough to withstand use in a harsh outdoor environment. The

image quality might also be degraded by environmental disturbances such as temperature drift, external electromagnetic noise, and strong wind. Furthermore, for long-term measurements, the radiofrequency (RF) probe should be adjustable or should be rebuilt to fit the target part of a tree, which grows and increases in size during the long measurement period.

For these reasons, only a few trials have been reported on *in situ* MRI measurements of plants living outdoors, although there are a number of studies in which flow mapping was measured by means of mobile nuclear magnetic resonance (NMR) devices in greenhouses and growth chambers but without imaging (see Ref. [3] for a review of such studies). The first application of NMR methods in measurement of xylem transport, although without imaging, was developed in 1984 [4]. The NMR-MOUSE (mobile universal surface explorer) [5,6] is a transportable NMR device that allows the detection of NMR signals from any part of a plant in surface proximity, although it is unsuitable for imaging because of the small homogenous field area. At present, the imaging of plants has been facilitated by using C-shaped permanent magnets with open-access designs with high sample accessibility and large homogenous magnetic fields that allow imaging of large trees. In 2000, Rokitta et al. [7] reported on a portable MRI system with the potential of imaging living plants in their natural environment, although they only performed indoor measurements and the imaging region was limited to the 12 mm diameter spherical volume. In 2006, Okada et al. [8] reported on the first outdoor MRI measurements of a living tree using a 0.3 T, 80 mm gap permanent magnet. In 2011, Kimura et al. [9] reported an electrically mobile MRI system with a flexible magnet-positioning system using the same

\* Corresponding author at: Institute of Applied Physics, University of Tsukuba, 1-1-1 Tennodai, Tsukuba, Ibaraki 305-8573, Japan. Fax: +81 29 853 5769.

E-mail address: [terada@bk.tsukuba.ac.jp](mailto:terada@bk.tsukuba.ac.jp) (Y. Terada).

magnet. They performed whole-day *in situ* measurements of the apparent diffusion coefficient and distinguished between healthy and diseased branches of a Japanese pear tree. In 2012, Jones et al. [10] reported on the ‘Tree Hugger,’ an open-access, transportable MRI system, for living trees using a 0.025 T, 210 mm gap magnet. They performed outdoor MRI measurements of a large tree for three months, and observed diurnal and seasonal changes in the water content across the stem using spin echo sequences. In 2013, Geya et al. [11] reported on longitudinal outdoor NMR measurements of a Japanese pear fruit using a 0.2 T, 160 mm gap magnet.

Meanwhile, MRI-based flow measurements [12–18], referred to as MRI flowmetry in this paper, refer to a frontier application that has potential in the study of water transport in plants at the cell level. The method of MRI flowmetry, based on propagator measurements [19–21] using the pulsed field gradient with stimulated echo (PFG-STE) or with spin echo (PFG-SE) sequences, has yielded unique information on the sap flow on a per-pixel basis [22–32]. There are also different types of examples of mobile devices that are capable of measuring flow but without imaging [33,34]. So far, however, MRI flowmetry has been performed on plants in laboratories only and not outdoors.

In this study, we developed an outdoor MRI system with an open-access permanent magnet that allows MRI flowmetry of an intact tree. We performed long-term MRI flowmetry outdoors, and found diurnal changes in the flow dynamics.

## 2. Materials and methods

### 2.1. MRI hardware and tree

The MRI system consisted of a 0.2 T, 160 mm gap permanent magnet (NEOMAX Engineering, Tokyo, Japan), a gradient coil set, an RF probe, and an MRI console. The magnet (Fig. 1(a)) was the same as in Ref. [35]. The specifications of the magnet are listed in Table 1. Fig. 1(b)–(d) shows the installation of the RF probe. First, the RF coil (15 turns, 60 mm length) was wound around a grooved plastic frame mounted on the tree stem (Fig. 1(b)). Next, the RF coil was shielded by an RF box made of 1 mm-thick acrylic plates and a 0.1 mm-thick Cu foil (Fig. 1(c)). Finally, to reduce the external electromagnetic noise, the RF probe was covered by a three-layer Al foil (40  $\mu\text{m}$  thick) (Fig. 1(d)).

The magnet, gradient coil set, RF probe, and other electronics were waterproofed by using a box made of acrylic plates (Fig. 1(e)) and covered by a vinyl sheet. The magnet temperature was kept almost constant by Si heaters and 8 mm-thick heat insulators made of polyethylene foam and Al sheet. To minimize the temperature drift, a temperature controller with proportional–integral–derivative controllers was used. As the magnet has a large heat capacity, the heat from the gradient coils would hardly affect the temperature control. The temperature drift of the magnet was  $\sim 0.3$  °C when the temperature outside the box changed by 10 °C, and the typical field drift was 1500 Hz/h (Fig. 1(f)). To compensate for the frequency drift, we used the field-frequency lock approach [36], in which the free induction decay (FID) was recorded at the beginning of the scan, and the base frequency was adjusted according with the Larmor frequency calculated from the FID signal. The field-frequency lock was performed at the beginning of the image acquisition with the interval of 7 min, during which the field drift was only 175 Hz.

We used the home-made gradient coil set (Fig. 1(g)). The  $z$ - (defined as the  $B_0$  direction) and  $y$ -gradient coils were the same as in Ref. [35], which were designed using the target field approach [37]. The  $x$ - (defined as the vertical direction) gradient coil was newly designed to maximize the gradient efficiencies

under the constraints of 10% gradient linearity using the genetic algorithm [38]. The specifications of the gradient coils are listed in Table 2. For the  $x$ -gradient, two layers of the same wire pattern were stacked in such a way as to double the efficiency. The gradients were not actively shielded, and the RF system did not allow Carr–Purcell–Meiboom–Gill (CPMG) sequences because of the large eddy currents, as will be discussed later. The offsetting on the  $x$ ,  $y$ , and  $z$  gradient coils were used to shim the field inhomogeneity.

The MRI console consisting of a transmitter (T145-5075 A, 100 W, 5–80 MHz, Thumway, Fuji, Japan), gradient driver (10 A, DST Inc., Asaka, Japan), MRI transceiver (DTRX-4, MRTechnology, Tsukuba Japan), and a personal computer, was placed in a roofed space (Fig. 1(h)). The total weight of the MRI console was about 100 kg. The console was also covered by a vinyl sheet.

The air temperature and relative humidity were measured at 10 min intervals with a sensor (TR-72WF, T and D Corp., Nagano, Japan) located inside a Stevenson screen placed 2 m away from the tree (Fig. 1(h)). The solar radiation was recorded at 5 min intervals with a sensor (ML-020S-O, Eko Instruments, Tokyo, Japan) located on the Stevenson screen. The volume of water content was recorded at 30 min intervals with a soil moisture sensor (SM300, Delta-T Devices, Cambridge, United Kingdom) buried at a depth of 20 cm from the ground surface.

We measured a *Zelkova serrata*, which is a ring-porous, deciduous tree. The tree was first planted, and the magnet was then placed such that the tree was located through the center of the magnet gap. A part of the trunk at 400 mm above ground was measured.

### 2.2. MRI measurements

The 2D spin-echo sequences with different echo times (TEs) and repetition times (TRs) (matrix size =  $128 \times 128$ , bandwidth = 25 kHz) were used to investigate the anatomical structures and the  $T_1$  and  $T_2$  relaxation times.

For flow measurements, we used PFG-STE (TE = 40 ms, TR = 800 ms, slice thickness = 40 mm, number of excitations (NEX) = 4, matrix size =  $128 \times 128$ , bandwidth = 25 kHz, field of view (FOV) = 120 mm  $\times$  120 mm, pixel size = 0.94 mm  $\times$  0.94 mm, duration of the two PFG pulses ( $\delta$ ) = 10 ms, and spacing of the two PFG pulses ( $\Delta$ ) = 100 ms). The amplitude,  $g$ , of the two PFG pulses was varied between  $-33.8$  and  $33.8$  mT/m at intervals of 4.23 mT/m, corresponding to the maximum  $q$  ( $q_{\text{max}}$ ) =  $1.44 \times 10^4$  m $^{-1}$  and  $\Delta q = 1.80 \times 10^3$  m $^{-1}$ , where  $q$  is defined as  $q = \gamma \delta g / 2\pi$  and  $\gamma$  is the gyromagnetic ratio of protons. The measurement time of one dataset (16 images with different  $q$  values) was about 2 h.

### 2.3. Flow analysis

The flow velocity was calculated from the  $q$ -space imaging (QSI) data on the basis of the propagator approach [24,25]. The QSI dataset were zero-filled to 32 sets at each point in the image space before Fourier transformation in  $q$ -space. For flow calibration, the phase of each QSI data was corrected using the first-order spatial polynomial fitting in such a way that the phases at four oil phantoms (4 mm in diameter) located outside the trunk were zero. Next, the propagator  $P(R, \Delta)$ , the probability distribution of displacement  $R$  in the direction of the PFGs within  $\Delta$ , was calculated on a per-pixel basis. The propagator was averaged spatially by using an average filter with a window size of  $3 \times 3$  to increase the apparent signal-to-noise ratio (SNR). The use of the larger window size lowered the spatial resolution greatly. The flow was evaluated from the propagator on the basis of the averaged window according to the following procedure. The fact that the stationary propagator is symmetrical around zero on the  $R$  axis was used to

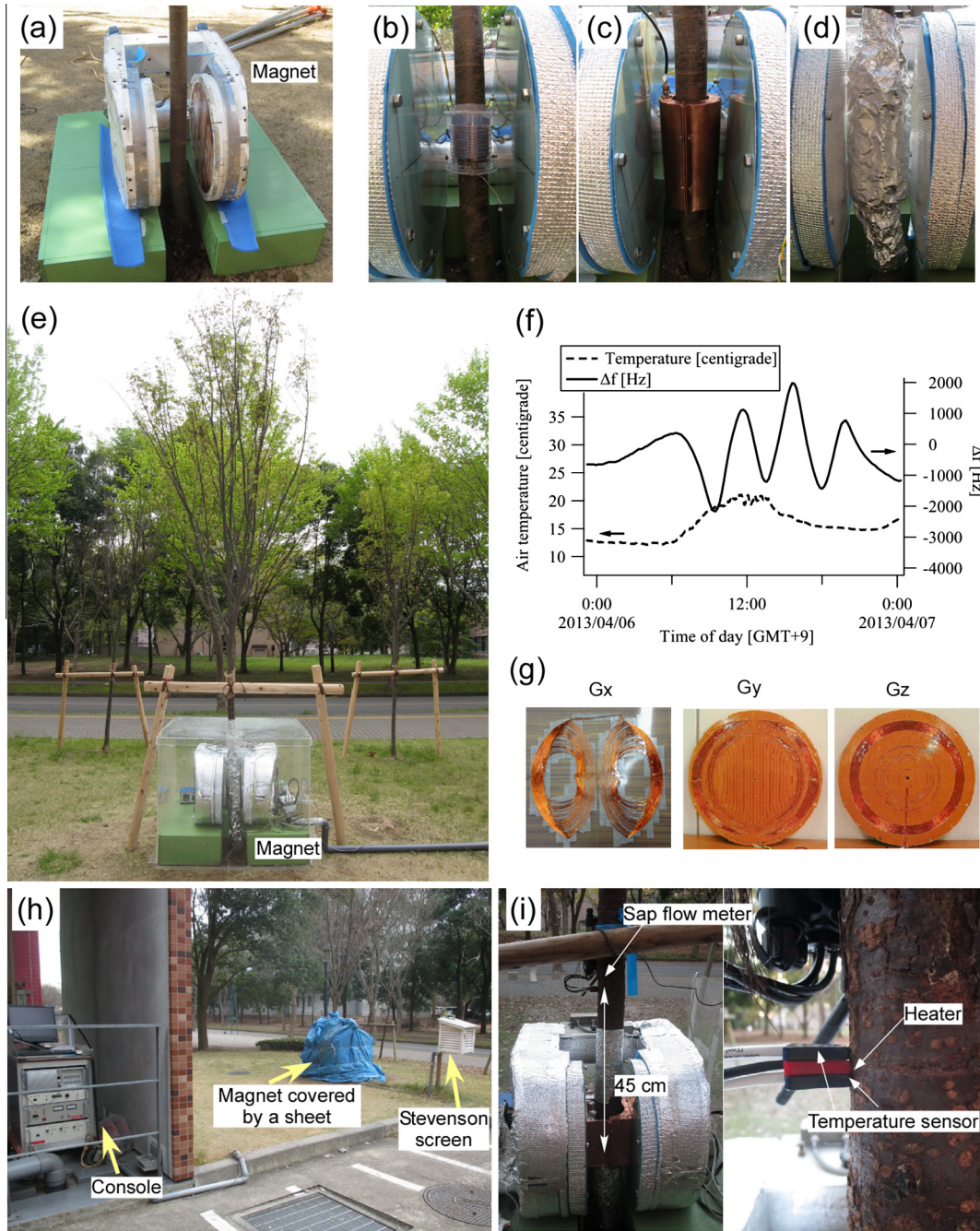


**Fig. 1.** The MRI system and the tree. (a) 0.2 T, C-shaped permanent magnet with a gap of 160 mm. (b–d) Installation of the RF probe. The RF coil was (b) wound on an acrylic frame attached to the trunk and (c) covered by the RF shield box. Next, the RF shield box was (d) covered by Al foil. (e) The waterproof system. The magnet, gradient coil set, RF probe, thermal control unit, and other electronics were waterproofed by a box made of acrylic plates. (f) Example of temporal variations of frequency shift  $\Delta f$  and air temperature. (g) Gradient coils.  $G_x$ : x-gradient coil,  $G_y$ : y-gradient coil,  $G_z$ : z-gradient coil. (h) MRI console and Stevenson screen where sensors of temperature, humidity, and solar radiation were placed. (i) Sap flow meter.

**Table 1**  
Specifications of magnet.

Magnet	
Field strength, T	0.2
Gap, mm	160
Weight, kg	520
Size, mm	700 (depth) $\times$ 500 (width) $\times$ 450 (height)
Nominal field homogeneity <sup>a</sup>	34.6 ppm over a 200 mm $\times$ 200 mm $\times$ 120 mm diameter ellipsoidal volume

<sup>a</sup> Peak-to-peak value.

separate stationary water from flowing water. Half of the propagator that did not include the flowing propagator was fitted to a half-Gaussian function. Next, the propagator in the non-flow direction was mirrored in the  $R$  axis and subtracted from the propagator in the flow direction. The remaining part of the propagator  $P_F(R, \Delta)$  represented the displacement distribution of the flowing water and was calibrated into  $P_C(R, \Delta)$  by dividing it by the average integral  $I_{ref}$  of propagators of pixels in the reference oil phantoms:

$$P_C(R, \Delta) = P_F(R, \Delta) / I_{ref}.$$

**Table 2**  
Specifications of the gradient coils.

Gradient coils	
Gap, mm	160
Target field region, mm	200 (x) × 200 (y) × 120 (z)
Diameter of current plane, mm	360
Number of turns of wire (x and y)	24
Number of turns of wire (z)	30
Current efficiency (x), mT/m/A	6.76
Current efficiency (y), mT/m/A	1.23
Current efficiency (z), mT/m/A	2.62
Maximum current efficiency (x), mT/m	67.6
Maximum current efficiency (y), mT/m	12.3
Maximum current efficiency (z), mT/m	26.2
Rise time (x), ms	1.2
Rise time (y), ms	0.8
Rise time (z), ms	0.8

The flow-conducting area per pixel,  $A$ , was calculated by adding propagator intensities multiplied by the pixel area,  $A_{\text{ref}}$ :

$$A = \sum_{R=0}^{R_{\text{max}}} P_C(R, \Delta) A_{\text{ref}}.$$

The volume flow per pixel  $Q$  was calculated as

$$Q = \sum_{R=0}^{R_{\text{max}}} (P_C(R, \Delta) R) A_{\text{ref}} / \Delta.$$

The average linear velocity per pixel,  $\bar{v}$ , was calculated as  $\bar{v} = Q/A$ . The stationary water area per pixel was calculated in the same way as the flow-conducting area per pixel but with the use of the complete Gaussian function generated from the half Gaussian fitted to the non-flow direction. In the flow maps, the upward flow is positive.

## 2.4. Simulation

We used the relatively small maximum of PFG because of the hardware limitation. This may cause truncation artifacts in the propagator and result in a large error in the flow estimation, particularly when the flow is slow. To confirm that this is not the case, we performed a simple simulation as follows. First, we considered a hypothetical propagator consisting of 70% stationary water and 30% flowing water at  $\Delta = 100$  ms. The propagators of stationary and flowing water were determined in such a way to mimic a typical flowing propagator measured in this study, as follows. The propagator of stationary water was assumed to follow a Gaussian curves with the standard deviation of 25  $\mu\text{m}$ . The propagator of flowing water was assumed to be a laminar flow with self-diffusion [22] that consisted of a rectangular function broadened by a Gaussian with the standard deviation of 25  $\mu\text{m}$ . Next the average linear velocity of hypothetical flowing water was determined by dividing half of the maximum displacement of the rectangular function by  $\Delta$ . Next, the Fourier transform of the hypothetical propagator was sampled with the same intervals and maximum of the  $q$ -values and 16 PFG steps as were used for the flow measurements. Finally, the sampled data were zero-filled and analyzed according to the flow analysis method described before. The errors between the simulated and hypothetical flow volumes were calculated as a function of the average linear velocity of flowing water. For comparison, the hypothetical propagator was sampled with the same intervals but with the larger numbers of maximum ( $q_{\text{max}} = 11.5 \times 10^4 \text{ m}^{-1}$ ) of the  $q$ -values and 128 PFG steps, and analyzed by the same procedure as described above.

## 2.5. Sap flow measurements

Sap flow was measured with a conventional sap flow meter (SFM1 Sap Flow Meter, ICT International, Armidale, Australia) using the heat ratio method (HRM) principle [39]. The temperature sensors and heater were inserted into the holes drilled in the stem at 450 mm above the center of the imaging volume (Fig. 1(i)). The sap flow velocity at 7.5 mm deep from the bark surface was measured at 10 min intervals. For sap velocity calibration, the thermal diffusivity of the fresh wood was set to be a nominal value of  $2.5 \times 10^{-3} \text{ cm}^2 \text{ s}^{-1}$ . The sap volume flow per pixel was calculated by multiplying the measured sap velocity by the pixel area.

## 3. Results

### 3.1. MR images of the growing tree

Fig. 2(a)–(f) presents spin echo images of the tree measured during almost two seasonal years from spring 2014. The SNRs of the images were high enough to visualize the anatomical structures, and the growth rings, which are a typical feature of ring-porous trees, were distinct in the images.

From spring to summer, the tree grew at a fast pace. The earlywood that developed during this period was observed as a large bright region in the summer (Fig. 2(b)). After summer, the growth speed decreased, and the latewood developed outside of the earlywood (Fig. 2(c)). From winter 2014 to spring 2015, the tree almost stopped growing, and there was only a slight increase in the diameter of the trunk. In winter 2014, the secondary phloem, which was located outside the latewood, was not distinguishable from the other regions, whereas in early spring 2015 (Fig. 2(d)), the phloem was imaged as a bright, ring-shaped structure in clear contrast with the other regions. From spring to late autumn 2015 (Fig. 2(e and f)), the tree grew in the same manner as in the previous year but at a faster pace.

Fig. 2(g) and (h) presents the relaxation-time maps measured in late autumn 2015. There was a large difference in relaxation time between latewood and earlywood. The  $T_1$  value was longer in the earlywood than in the latewood, and  $T_2$  also showed the same tendency. The observed difference would mainly result from the size difference in the water vessel. The relaxation time decreases with the size of the plant cell [29]. In general, the earlywood contains many more larger vessels than latewood, and this would result in the smaller decrease in relaxation time. Fig. 2(i) presents the magnification of the  $T_1$  image and the anatomical structures estimated from the relaxation maps. The earlywood regions that developed in 2014 and 2015 (EW2014 and EW2015) exhibited longer  $T_1$  values than the latewood regions that developed in the same timeframe (LW2014 and LW2015).

### 3.2. MR flowmetry in the late autumn

Fig. 3 shows the results of MRI flowmetry obtained in late autumn (November 28, 2015). The quantitative flow maps representing the average volume flow (Fig. 3(a)), flow conducting area (Fig. 3(b)), average linear velocity (Fig. 3(c)), and the stationary water (Fig. 3(d)) show a clear spatial difference in the stem. The shape and position of the xylem flow corresponds closely with the  $T_1$  and  $T_2$  images. In the volume flow map, the large upward flow was visible in EW2015 and the slight but nonnegligible flow also appeared in EW2014. The average volume flow over EW2015 was  $7.6 \times 10^{-2} \text{ mm}^3 \text{ s}^{-1}$ . The standard deviation of the volume flow over the reference phantom region was  $1.8 \times 10^{-2} \text{ mm}^3 \text{ s}^{-1}$ , which gives a rough estimation of the noise level in the

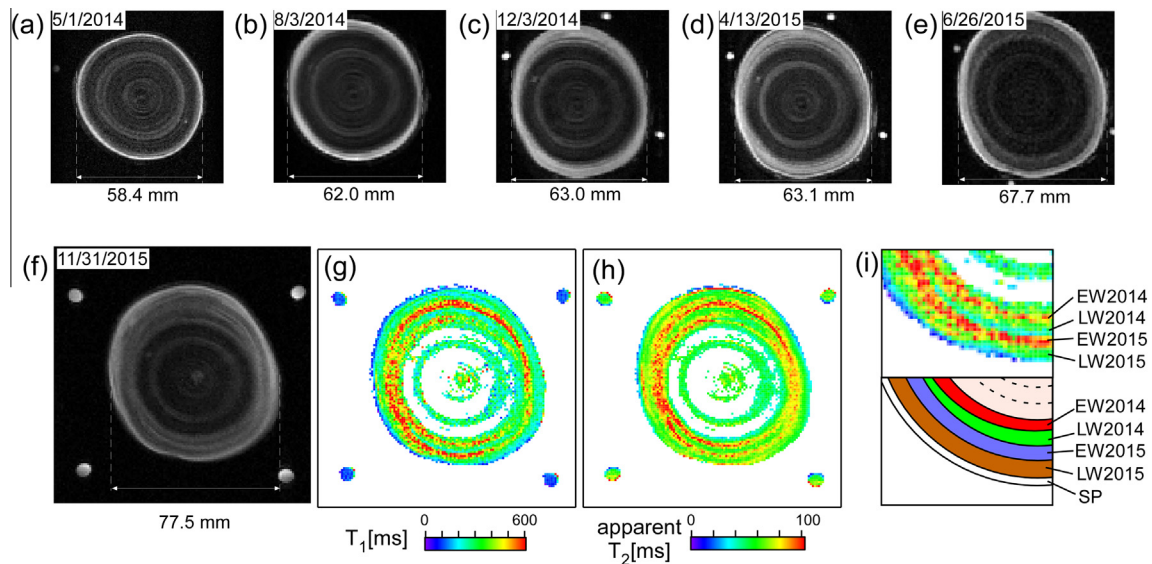


**Fig. 2.** MR images of the growing tree. (a)–(f) Spin echo images obtained on (a) 5/1/2014, (b) 8/3/2014, (c) 12/3/2014, (d) 4/13/2015 (e) 6/26/2015, and (f) 11/31/2015; TE/TR = 20 ms/800 ms. (a) FOV = 80 mm × 80 mm; (b)–(e) original FOV = 100 mm × 100 mm, and the margins of the images were cut. The size of the final images was 80 mm × 80 mm. (f) FOV = 120 mm × 120 mm. (g) and (h)  $T_1$  and apparent  $T_2$  images obtained on 11/30/2015. The slice thickness was 40 mm. The spin echo images with TE = 20 ms and TR = 200, 400, 800, 1200, and 3000 ms were used for the  $T_1$  calculation, and with TE = 20, 30, 40, 50, and 60 ms, and TR = 1200 ms were used for the apparent  $T_2$  calculation. (i) Magnification of the  $T_1$  image and schematic of ring-porous structures estimated from the  $T_1$  images. EW2014 and EW2015: earlywoods developed in 2014 and 2015, LW2014 and LW2015: latewoods developed in 2014 and 2015, SP: secondary phloem.

volume flow map. The average linear velocity over EW2015 was 0.65 mm/s.

The pixel propagator at the position showing almost maximum flow volume is depicted in Fig. 3(e). The measured flowing propagator ranged below  $R = 200 \mu\text{m}$  and no wraparound was observed on the  $R$  axis.

### 3.3. Simulation result

The simulation results performed under conditions similar to the experimental conditions are shown in Fig. 4. The hypothetical propagator (Fig. 4(a)) and its Fourier transform shows truncation at  $q = q_{\text{max}}$  (Fig. 4(b)) because the signal was not sufficiently attenuated. Although this caused a ringing artifact in the simulated total propagator (Fig. 4(c)), the analyzed flowing propagator was less affected by the artifact. The errors between the hypothetical and simulated flow volumes were within about 10% for  $N = 16$  (where  $N$  is the number of sampling points), if the average linear velocity was above 0.15 mm/s. This threshold velocity could give a rough estimation for the lower limit of the flow velocity detectable under this particular experimental condition.

### 3.4. Diurnal flow variation

Fig. 5 shows the diurnal variations of the average volume flow. The volume flow maps measured at midday on different days show a gradual decrease with passing time (Fig. 5(a)–(g)). This feature is also clearly seen in Fig. 5(h), which shows the volume flow averaged over entire xylem regions (including EW2014, LW2014, EW2015, and LW2015). The flow volume changed periodically within the day and it was high during daytime and low at night.

The sap flow volume measured with the conventional sap flow meter (Fig. 5(i)) showed the same time dependency as the flow volume measured by QSI (Fig. 5(h)), although there was a slight difference in magnitude. The flow volumes measured by QSI and the sap flow meter correlated well with each other (Pearson's  $r = 0.82$ ,  $P < 0.0001$ ).

Fig. 5(j and k) shows pictures of branches taken during the measurement times. The tree was a deciduous tree that did not have any leaves during winter. There were many leaves remaining on the branches in earlier days (Fig. 5(j)) and they fell mostly in later days (Fig. 5(k)). This would cause the gradual decrease in the flow volume, because leaf transpiration is a major driving force for xylem flow.

The detailed diurnal and spatial variations in volume flow and their relationships with meteorological data are presented in Fig. 6. The flow changed rather uniformly depending on the time of day (Fig. 6(a–d and f)). The flow volume was the largest in EW2015, and was almost the same as in the other xylem regions. The flow volume correlated well with the temperature, relative humidity, and volume water content.

## 4. Discussion

We have successfully demonstrated *in situ* MRI-flow measurements for a tree living in the outdoors. To our knowledge, this is the first report on MRI flowmetry performed on an outdoor tree. To achieve this, we overcame several of the difficulties of making long-term, outdoor MRI measurements of a living tree.

First, the MRI hardware should be protected to withstand use in a harsh outdoor environment that often changes rapidly and drastically. In our system, the MRI hardware including the magnet, gradient coils, RF probes, and electronic instruments were covered by an acrylic box and vinyl sheet, and this protection was sufficient for long-term use outdoors. Second, the RF probe should be adjustable to fit a plant that is growing and increasing in size. To adjust for the growing tree, we changed RF probes four times during the two-year measurement period. The third issue was the temperature drift of the permanent magnet. The NdFeB permanent magnet used in this system had a large thermal coefficient about  $-1000$  ppm/degree. The large temperature change outdoors may lead to a large  $B_0$  drift and may result in image artifacts or failure in drift compensation using the field-frequency lock approach. The magnet used in our system was thermally insulated by a polyethylene sheet attached to the magnet and by the plastic case waterproofing

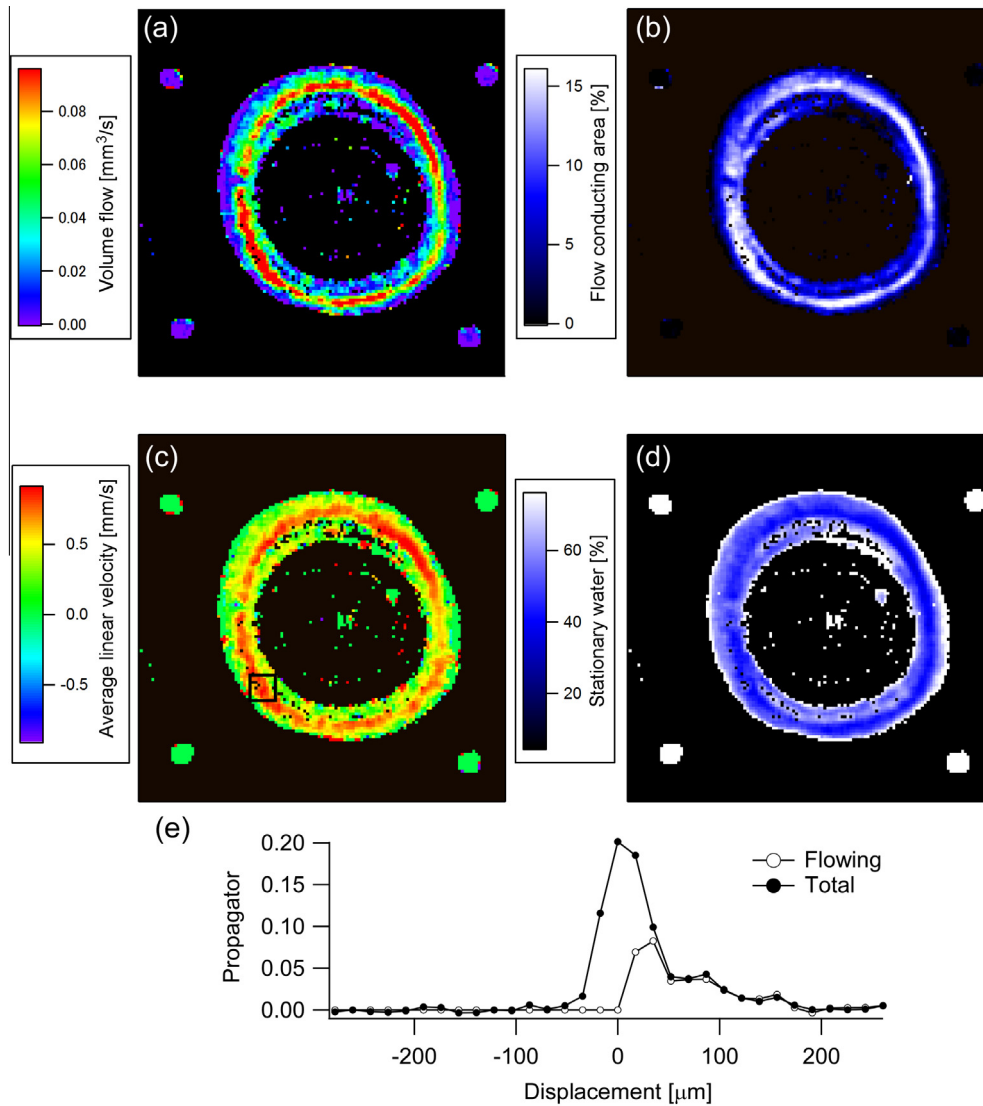


**Fig. 3.** Results of MRI flowmetry measured in late autumn (11/28/2015). (a) Volume flow. (b) Flow-conducting area. (c) Average linear velocity. (d) Amount of stationary water. (e) Propagators measured at the position indicated by the black square in (c).

the magnet and the electronics. This insulating system resulted in a small temperature drift of the magnet. To overcome this small temperature drift, the field-frequency locking was used to enable artifact-free imaging. Fourth, the external noise coming through the tree might have caused artifact lines on spin-echo images corresponding to the frequencies of the noise. In our system, the Al foils covering the tree trunk reduced the external noise effectively, and no artifact lines appeared on the images. Finally, the field homogeneity may suffer during the transportation of the magnet or be degraded during prolonged use because of the deterioration of the magnetic materials. Although it was difficult to measure the actual homogeneity, the overall image qualities were unchanged during the two years of measurements, which demonstrates that the homogeneity remained sufficiently high.

The robustness of the system was demonstrated by the long-term measurement of spin-echo imaging (Fig. 2). Latewood, earlywood, and phloem were identified using the time series images and relaxation time maps. It should be noted that we used relatively long TE values for the  $T_2$  measurement and the measured  $T_2$  values were different from the true  $T_2$  of the sample. In plants, there are a large number of air-water interfaces around cells, which causes large local gradients because of susceptibility

variation. This effect contributes to the measured  $T_2$  values [29], and therefore the information presented in the  $T_2$  image is mostly called 'apparent'. To avoid susceptibility effects, TE values should be as short as possible, typically <5 ms. It should also be noted that the longest  $T_1$  value in the tree was around 600 ms, which was close to the repetition time (800 ms) for flow measurements. Therefore, the signal amplitude of flowing water could be fairly saturated, although this does not affect the final results of MRI flowmetry.

The flow measurements yielded reliable information on sap flow that has potential to characterize the underlying plant physiology. The measured flow characteristic showed the pronounced features that are consistent with the standard model [40] for water flow in ring-porous trees. The xylem flow occurred mainly in the earlywood that has developed in 2015, which had the youngest and most active large vessels. When there were many leaves left on the branches (before December 1, 2015), the xylem flow showed clear patterns of enhanced transport during the day and strong flow reduction at night. Furthermore, the diurnal change in flow correlated well with the metrological data. The flow was fastest at the midday when the driving force for transpiration was the highest, relative humidity was the lowest, and the vapor

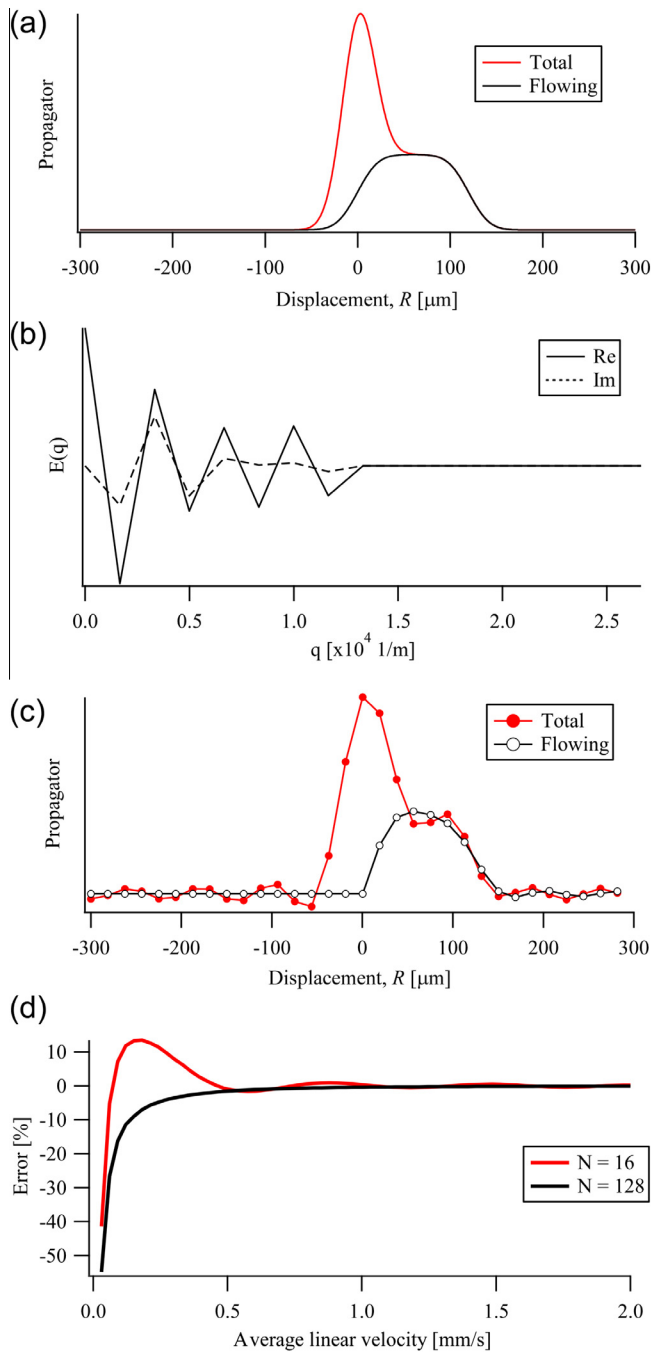


**Fig. 4.** Simulation of propagators. (a) Hypothetical propagator consisting of 70% stationary water (standard deviation = 25  $\mu\text{m}$ ) and 30% flowing water (half maximum displacement of the rectangular function = 60  $\mu\text{m}$ , standard deviation = 25  $\mu\text{m}$ , which corresponds to the displacement of flowing water at  $\Delta = 100$  ms with 0.6 mm/s average linear velocity). (b) Fourier transform  $E(q)$  of the hypothetical propagator shown in (a). (c) Simulated propagator obtained by sampling the hypothetical propagator with the same intervals and maximum of the  $q$ -values and 16 PFG steps as were used for the flow measurements. (d) Estimated errors in flow volume between the hypothetical and simulated propagators. In each simulation, the center position of the hypothetical propagator at time  $\Delta = 100$  ms was calculated from the average linear velocity.  $N$  is the number of sampling points.

pressure deficit was the largest. As the leaves fell, the measured xylem flow showed a clear reduction. Furthermore, all these features correlated well with the results obtained with the conventional sap flow meter.

For the flow measurements based on a propagator using PFG sequences, we used the limited maximum of the PFG steps. This

may cause truncation artifacts in the propagators, if the signal is not completely attenuated by the PFGs. The limited PFG maximum also limits the resolution of the flow profile in the propagator, which may lead to insufficient separation of the flowing and stationary water. Such artifacts may cause serious problems in subsequent data evaluation. However, this was unlikely to occur in this study for the following reasons. The propagators simulated under the current experimental settings showed that errors between the hypothetical and simulated flow volumes were below 10% for the average linear velocity above 0.15 mm/s, and this error might be tolerated for the measurement of the xylem flow, at least in this season. In addition, as described in the previous paragraph, the measured flow showed the pronounced features of the standard flow model of ring-porous trees. There was also a good quantitative agreement in the flow volume measured with the propagator method and conventional sap flow meter. All these facts support the validity of the proposed method.

The low number of PFG steps may also result in aliasing in the propagator and might limit the displacement that can be measured at a given maximum of PFGs. This occurs if the flow is faster than a threshold determined by  $1/\Delta q$  and the flow encoding time  $\Delta$ . A much faster flow would ultimately lead to a smearing out of the signal over the width of the propagator. This was not the case in late autumn when there were not so many leaves in the branches, as confirmed by the propagators (Fig. 3(e)). However, under conditions of high transpiration, the flow was likely to be faster and exceed the upper detection limit under the current experimental setting. The xylem sap flow velocities that have been reported reach several mm/s at midday in the summer [25,26]. To measure such fast flows, it is necessary to start with an experiment tailored to measure fast flowing water (using a short  $\Delta$ ), then after establishing how fast the fastest flowing water moved, adjust the flow encoding settings accordingly. There is another issue to be considered. In a ring-porous tree, there are wide vessels that will conduct fast bulk flow and many narrow vessels that will contain much slower flowing water. The measurement of such widely-distributed flows may require a larger maximum of PFGs that would enable sufficient separation of the flowing and stationary water. In this case, the number of PFG steps should also be larger to maintain the upper detection limit of the flow velocity. This may lead to an increase in the effective measurement time and use of fast sequences such as fast spin echo [24,25] might be needed to maintain the sufficiently high temporal resolution of flow measurements.

The flow in the phloem was not observed in this study. It has been reported that the phloem flow velocities are in the order of about hundreds of  $\mu\text{m/s}$  [25,26]. Although the phloem flow velocity in the tree was unknown, it would be below the detectable limit under the current experimental setting. To measure phloem transport, it is necessary to use larger  $\Delta$  values to separate such slow flows from stationary water. However, this increases the risk of aliasing in the propagator of fast xylem flow. Therefore, the xylem and phloem flows should be measured separately with different flow encoding sets. Moreover, a more elaborate strategy may be needed to ensure the SNR of phloem flow measurements. It has been reported that it was usually necessary to lower spatial resolution, take many averages per individual measurements, or alternatively to sum the information originating from all flow-containing pixels in an image into a one-dimensional flow profile [25].

The flow volume measured by QSI was about three times larger than that measured by HRM (Fig. 5(h and i)). In the MRH, the flow was measured at the position where the thermistor was located, and the misalignment of the thermistor could significantly affect the accuracy of measurement. In this study, the thermistor position was determined to be located at the fast-flowing xylem region

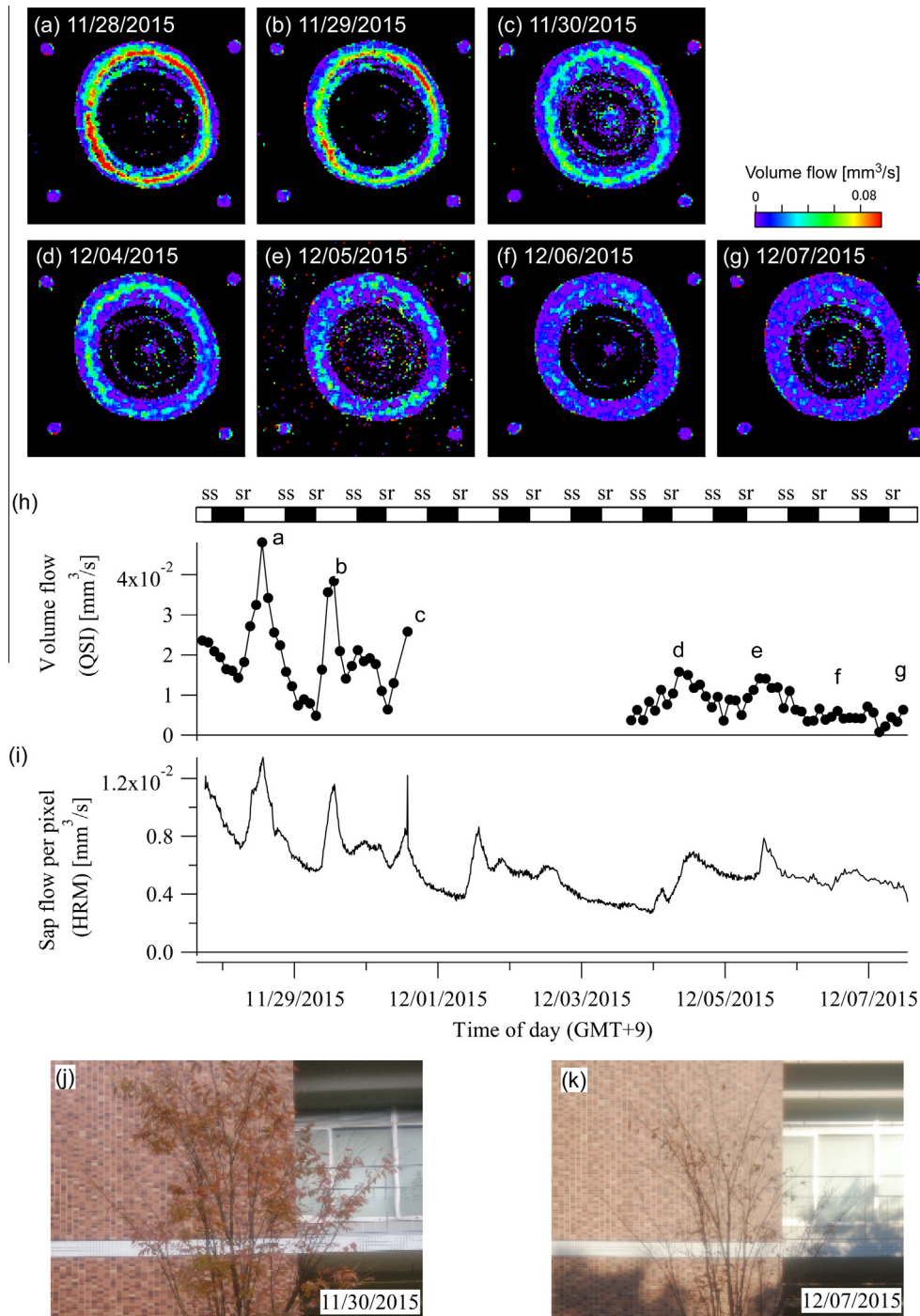


**Fig. 5.** Daily patterns of flow measured in late autumn (from 11/28/2015 to 12/07/2015). (a–g) Volume flow measured at midday. (h) Volume flow averaged over the whole region of xylem developed in 2014 and 2015. The lateral axis is the same as that in (i). The times of sunset (ss) and sunrise (sr) are plotted on the upper axis. EW is earlywood, LW is latewood, SP is secondary phloem. (i) Sap flow measured with the conventional sap flow meter utilizing the heat ratio method (HRM) principle. (j and k) Photos of leaves taken at midday on the date indicated.

with the aid of the MR images. However, the bark was hardly imaged and its thickness was unknown, which may result in the misalignment of the thermistor in the radial direction. Moreover, the area measured by the HRM was 450 mm above the center of the imaging volume of MRI, where the anatomical structures could not be imaged. In addition, the thermal diffusivity used to derive the sap velocity was uncorrected. All these factors would be responsible for the measured difference in flow volumes. Despite these factors, the flow pattern measured by QSI correlated well

with that measured by HRM, which demonstrates the validity of the flow measurement using QSI.

There are other technical limitations in this work. The first one is that a replacement of the RF probe was necessary to adjust with the growing tree. In this work, we started to fabricate the new, alternative probe after the old probe was broken. The probe fabrication and installation resulted in the interruption of the long-term measurements for about a month. Prediction of the dimensions of the new probe would reduce interruption time. Second, the region

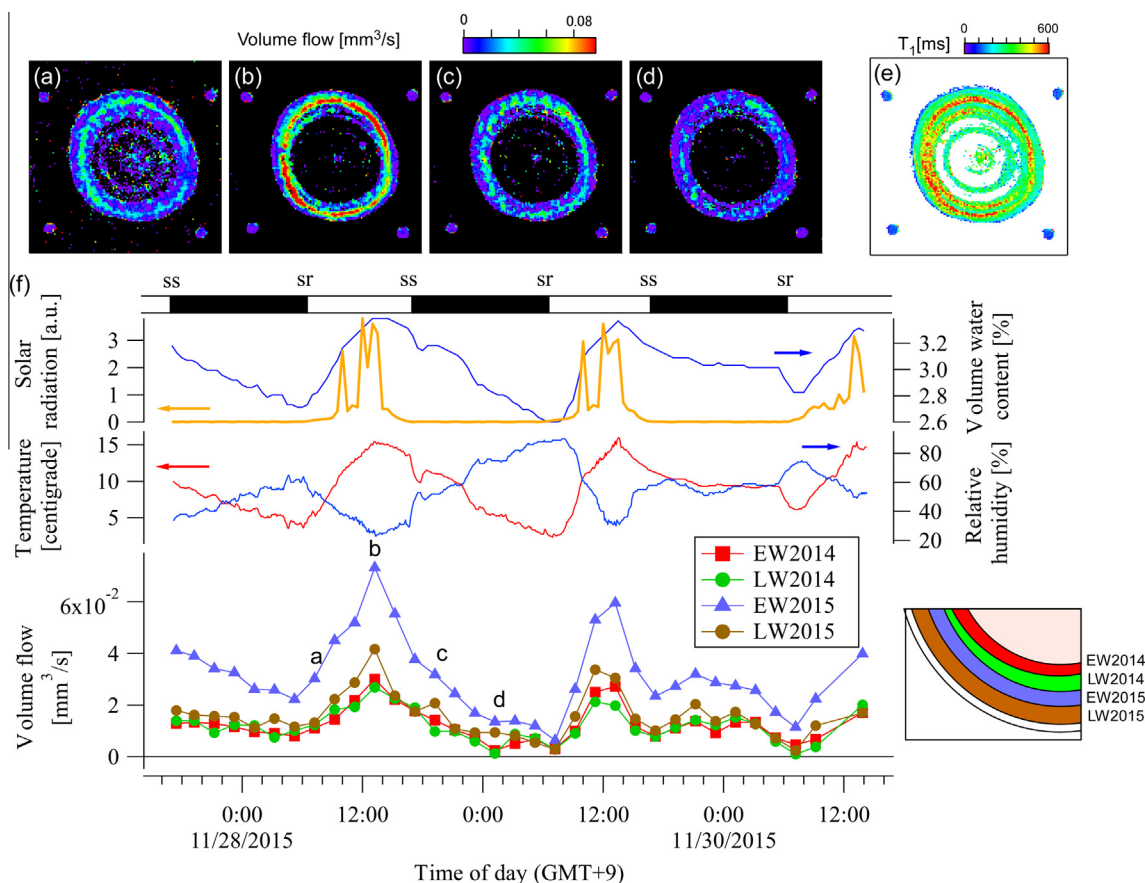


**Fig. 6.** Diurnal pattern of flow. (a–d) Volume flow measured at different times of the day. (The respective measurement times are indicated on the bottom graph in (f)). (e)  $T_1$  map for reference (identical to Fig. 2(g)). (f) Volume flow averaged in the xylem regions that grew in 2014 and 2015 and plots of temperature, relative humidity, solar radiation, and volume water content for the same days. The times of sunset (ss) and sunrise (sr) are plotted on the upper axis. EW2014 and EW2015 are earlywood developed in 2014 and 2015, respectively; LW 2014 and LW2015 are latewood developed in 2014 and 2015, respectively.

to be imaged was limited to a part of the stem at several tens of centimeters above the ground. The third issue was the ghosting artifact arising from the strong wind. Currently, all the images were checked visually, and those with severe ghosting artifacts were not used for the QSI analysis. This issue also caused the dead time between the measurements. The alternative schemes with the motion-insensitive data acquisition such as radial and projection acquisitions would reduce the presence of the ghosting artifacts. Fourth, the maximum gradient strength was not sufficient for measuring the high flow velocities that one could expect in summer, when the tree is transpiring at full force. Stacking more gradient coils with the same coil patterns or the use of a more powerful gradient driver would solve this issue. The fifth issue was the disability of acquiring multiple echoes. For this reason, true  $T_2$  measurements with CPMG sequences and fast flow imaging with FSE sequences are currently not feasible. This problem would originate from large phase mismatching in the RF pulses because of large eddy currents on conductive structures, such as the aluminum sheets, shielding box, and ferromagnetic materials. To overcome this limitation, the use of actively-shielded gradient coils and pre-emphasis techniques [41] may be efficient.

Finally, we discuss the choice of the magnet and field strength for plant imaging in the outdoors. In this study, we used a 0.2 T, large magnet with the open design. The openness made it easy to set the magnet around the tree trunk that had been planted and to replace the RF probe. The large imaging volume allowed us to image the large tree. However, this has also resulted in a heavy magnet, and it was difficult to probe plant stems, and tree branches

with varied and irregular diameters, shapes and orientations using this magnet. The use of a light, mobile MRI system with a flexible positioning and rotation mechanism [9,34] would overcome this issue at the cost of the available imaging volume.

The field strength of 0.2 T was sufficiently high for performing the routine flow imaging. It was demonstrated that the measured flow maps have sufficient image quality and temporal resolution to clarify the diurnal variations of flow dynamics. The use of magnets with higher field strength would lead to a higher SNR, higher spatial resolution, and shorter measurement time. The field strength of an open permanent magnet is limited to 1.0 T, and close magnets have a higher field strength, up to 2.0 T. However, there is in general a tradeoff between available imaging volume and field strength, and the use of the 0.2 T permanent magnet was the optimal choice for our purpose. Superconducting magnets also have high field strengths, but running a superconducting magnet MRI system for a living tree in the outdoors remains a tremendous challenge.

## 5. Conclusion

We have developed an MRI system for outdoor measurements of a living tree to study water dynamics. The system was robust enough for long-term measurements. The anatomical structures including latewood, earlywood, and phloem were identified using the time-series MR images and relaxation-time maps. The MRI-flow measurements demonstrated the diurnal changes in flow velocity in the xylem on a per-pixel basis. We have concluded that

our outdoor MRI system is a powerful tool for studies on water transport and the physiological processes of plants growing in the natural environment.

### Acknowledgment

The authors would like to thank Dr. Kenji Fukuda for his helpful comments on the manuscript and for his kind permission to use the sap flow meter.

### References

- [1] H. Van As, J. Van Duynhoven, MRI of plants and food, *J. Magn. Reson.* 229 (2013) 25–34.
- [2] L. Borisjuk, H. Rolletschek, T. Neuberger, Surveying the plant's world by magnetic resonance imaging, *Plant J.* 70 (2012) 129–146.
- [3] W. Köckenberger, Functional imaging of plants by magnetic resonance experiments, *Trends Plant Sci.* 6 (2001) 286–292.
- [4] H. Van As, T.J. Schaafsma, Noninvasive measurement of plant water flow by nuclear magnetic resonance, *Biophys. J.* 45 (1984) 462–472.
- [5] G. Eidmann, R. Savelsberg, P. Blümmler, B. Blümich, The NMR MOUSE, a mobile universal surface explorer, *J. Magn. Reson.* 122 (1996) 104–109.
- [6] B. Blümich, P. Blümmler, G. Eidmann, A. Guthausen, R. Haken, U. Schmitz, K. Saito, G. Zimmer, The NMR-mouse: construction, excitation, and applications, *Magn. Reson. Imag.* 16 (1998) 479–484.
- [7] T. Rokitta, E. Rommel, U. Zimmermann, A. Haase, Portable nuclear magnetic resonance imaging system, *Rev. Sci. Instrum.* 71 (2000) 4257–4262.
- [8] F. Okada, S. Handa, S. Tomiha, K. Ohya, K. Kose, T. Haishi, S. Utsuzawa, K. Togashi, Development of a portable MRI for outdoor measurements of plants, in: *The Sixth Colloquium on Mobile Magnetic Resonance*, Aachen, Germany, 6–8 September, 2006.
- [9] T. Kimura, Y. Geya, Y. Terada, K. Kose, T. Haishi, H. Gemma, Y. Sekozawa, Development of a mobile magnetic resonance imaging system for outdoor tree measurements, *Rev. Sci. Instrum.* 82 (2011) 053704.
- [10] M. Jones, P.S. Aptaker, J. Cox, B.A. Gardiner, P.J. McDonald, A transportable magnetic resonance imaging system for in situ measurements of living trees: the Tree Hugger, *J. Magn. Reson.* 218 (2012) 133–140.
- [11] Y. Geya, T. Kimura, H. Fujisaki, Y. Terada, K. Kose, T. Haishi, H. Gemma, Y. Sekozawa, Longitudinal NMR parameter measurements of Japanese pear fruit during the growing process using a mobile magnetic resonance imaging system, *J. Magn. Reson.* 226 (2013) 44–51.
- [12] E. Kuchenbrod, M. Landeck, F. Thürmer, A. Haase, U. Zimmermann, Measurement of water flow in the xylem vessels of intact maize plants using flow-sensitive NMR imaging, *Bot. Acta* 109 (1996) 184–186.
- [13] W. Köckenberger, J.M. Pope, Y. Xia, K.R. Jeffrey, E. Komor, P.T. Callaghan, A non-invasive measurement of phloem and xylem water flow in castor bean seedlings by nuclear magnetic resonance microimaging, *Planta* 201 (1997) 53–63.
- [14] E. Kuchenbrod, E. Kahler, F. Thürmer, R. Deichmann, U. Zimmermann, A. Haase, Functional magnetic resonance imaging in intact plants – quantitative observation of flow in plant vessels, *Magn. Reson. Imag.* 16 (1998) 331–338.
- [15] M. Rokitta, U. Zimmermann, A. Haase, Fast NMR flow measurements in plants using FLASH imaging, *J. Magn. Reson.* 137 (1999) 29–32.
- [16] M. Rokitta, A.D. Peuke, U. Zimmermann, A. Haase, Dynamic studies of phloem and xylem flow in fully differentiated plants by fast nuclear-magnetic-resonance microimaging, *Protoplasma* 209 (1999) 126–131.
- [17] A.D. Peuke, M. Rokitta, U. Zimmermann, L. Schreiber, A. Haase, Simultaneous measurement of water flow velocity and solute transport in xylem and phloem of adult plants of *Ricinus communis* over a daily time course by nuclear magnetic resonance spectrometry, *Plant, Cell Environ.* 24 (2001) 491–503.
- [18] U. Tallarek, T.W.J. Scheenen, P.A. de Jager, H. Van As, Using NMR displacement imaging to characterize electroosmotic flow in porous media, *Magn. Reson. Imag.* 19 (2001) 453–456.
- [19] P.T. Callaghan, C.D. Eccles, Y. Xia, NMR microscopy of dynamic displacements: k-space and q-space imaging, *J. Phys. E: Sci. Instrum.* 21 (1988) 820–822.
- [20] T.J. Schaafsma, H. Van As, W.D. Palstra, J.E.M. Snaar, P.A. De Jager, Quantitative measurement and imaging of transport processes in plants and porous media by <sup>1</sup>H NMR, *Magn. Reson. Imag.* 10 (1992) 827–836.
- [21] P.T. Callaghan, W. Köckenberger, J.M. Pope, Use of difference propagators for imaging of capillary flow in the presence of stationary fluid, *J. Magn. Reson. B* 104 (1994) 183–188.
- [22] T.W.J. Scheenen, D. van Dusschoten, P.A. de Jager, H. Van As, Quantification of water transport in plants with NMR imaging, *J. Exp. Bot.* 51 (351) (2000) 1751–1759.
- [23] T.W.J. Scheenen, D. van Dusschoten, P.A. de Jager, H. Van As, Microscopic displacement imaging with pulsed field gradient turbo spin-echo NMR, *J. Magn. Reson.* 142 (2000) 207–215.
- [24] T.W.J. Scheenen, F.J. Vergeldt, C.W. Windt, P.A. de Jager, H. Van As, Microscopic imaging of slow flow and diffusion: a pulsed field gradient stimulated echo sequence combined with turbo spin echo imaging, *J. Magn. Reson.* 151 (2001) 94–100.
- [25] C.W. Windt, F.J. Vergeldt, P.A.D. Jager, H. Van As, MRI of long-distance water transport: a comparison of the phloem and xylem flow characteristics and dynamics in poplar, castor bean, tomato and tobacco, *Plant, Cell Environ.* 29 (2006) 1715–1729.
- [26] A.D. Peuke, C. Windt, H. Van As, Effects of cold-girdling on flows in the transport phloem in *Ricinus communis*: is mass flow inhibited?, *Plant, Cell Environ.* 29 (2006) 15–25.
- [27] H.M. Homan, C.W. Windt, F.J. Vergeldt, E. Gerkema, H. Van As, 0.7 and 3 T MRI and sap flow in intact trees: xylem and phloem in action, *Appl. Magn. Reson.* 32 (2007) 157–170.
- [28] T.W.J. Scheenen, F.J. Vergeldt, A.M. Heemskerk, H. Van As, Intact plant magnetic resonance imaging to study dynamics in long-distance sap flow and flow-conducting surface area, *Plant Physiol.* 144 (2007) 1157–1165.
- [29] H. Van As, Intact plant MRI for the study of cell water relations, membrane permeability, cell-to-cell and long-distance water transport, *J. Exp. Bot.* 58 (2007) 743–756.
- [30] C.W. Windt, E. Gerkema, H. Van As, Most water in the tomato truss is imported through the xylem, not the phloem: a nuclear magnetic resonance flow imaging study, *Plant Physiol.* 151 (2009) 830–842.
- [31] D.L. Mullendore, C.W. Windt, H. Van As, M. Knoblauch, Sieve tube geometry in relation to phloem flow, *Plant Cell* 22 (2010) 579–593.
- [32] A.D. Peuke, A. Gessler, S. Trumbore, C.W. Windt, N. Homan, E. Gerkema, H. Van As, Phloem flow and sugar transport in *Ricinus communis* L. is inhibited under anoxic conditions of shoot or roots, *Plant, Cell Environ.* 38 (2015) 433–447.
- [33] F. Casanova, J. Perlo, B. Blümich, Velocity distributions remotely measured with a single-sided NMR sensor, *J. Magn. Reson.* 171 (2004) 124–130.
- [34] C.W. Windt, H. Soltner, D. van Dusschoten, P. Blümmler, A portable Halbach magnet that can be opened and closed without force: the NMR-CUFF, *J. Magn. Reson.* 208 (2011) 27–33.
- [35] S. Handa, H. Yoshioka, S. Tomiha, T. Haishi, K. Katsumi, Optimized system design and construction of a compact whole-hand scanner for diagnosis of rheumatoid arthritis, *Magn. Reson. Med. Sci.* 6 (2007) 113–120.
- [36] T. Haishi, T. Uematsu, Y. Matsuda, K. Kose, Development of a 1.0 T MR microscope using a Nd–Fe–B permanent magnet, *Magn. Reson. Imag.* 19 (2001) 875–880.
- [37] R. Turner, A target field approach to optimal coil design, *J. Phys. D: Appl. Phys.* 19 (1986) 147–151.
- [38] B.J. Fisher, N. Dillon, T.A. Carpenter, L.D. Hall, Design of a biplanar gradient coil using a genetic algorithm, *Magn. Reson. Imag.* 15 (1997) 369–376.
- [39] S.S.O. Burgess, M.A. Adams, N.C. Turner, C.R. Beverly, C.K. Ong, A.A.H. Khan, T. M. Bleby, An improved heat pulse method to measure low and reverse rates of sap flow in woody plants, *Tree Physiol.* 21 (2001) 589–598.
- [40] L. Taiz, E. Zeiger, *Plant Physiology*, Sinauer Associates, Inc., Sunderland MA.
- [41] F.G. Goora, B.G. Colpitts, B.J. Balcom, Arbitrary magnetic field gradient waveform correction using an impulse response based pre-equalization technique, *J. Magn. Reson.* 238 (2014) 70–76.